Ultraquantum magnetoresistance in the Kramers-Weyl semimetal candidate β-Ag_2Se

Cheng-Long Zhang,[1] Frank Schindler,[2] Haiwen Liu,[3] Tay-Rong Chang,[4] Su-Yang Xu,[5] Guoqing Chang,[6,7] Wei Hua,[8] Hua Jiang,[9] Zhujun Yuan,[1] Junliang Sun,[8] Horng-Tay Jeng,[4,10] Hai-Zhou Lu,[11] Hsin Lin,[6,7] M. Zahid Hasan,[5] X. C. Xie,[1,12] Titus Neupert,[2] and Shuang Jia[1,12,*]

[1]*International Center for Quantum Materials and School of Physics, Peking University, Beijing 100871, China*
[2]*Department of Physics, University of Zurich, Winterthurerstrasse 190, 8057 Zurich, Switzerland*
[3]*Center for Advanced Quantum Studies, Department of Physics, Beijing Normal University, Beijing 100875, China*
[4]*Department of Physics, National Tsing Hua University, Hsinchu 30013, Taiwan, Republic of China*
[5]*Joseph Henry Laboratory, Department of Physics, Princeton University, Princeton, New Jersey 08544, USA*
[6]*Centre for Advanced 2D Materials and Graphene Research Centre, National University of Singapore, 6 Science Drive 2, Singapore 117546*
[7]*Department of Physics, National University of Singapore, 2 Science Drive 3, Singapore 117542*
[8]*Department of Chemistry, Peking University, Beijing 100871, China*
[9]*College of Physics, Optoelectronics and Energy, Soochow University, Suzhou 215006, China*
[10]*Institute of Physics, Academia Sinica, Taipei 11529, Taiwan, Republic of China*
[11]*Department of Physics, South University of Science and Technology of China, Shenzhen 518055, China*
[12]*Collaborative Innovation Center of Quantum Matter, Beijing 100871, China*

(Received 7 August 2017; published 26 October 2017)

The topological semimetal β-Ag_2Se features a Kramers-Weyl node at the origin in momentum space and a quadruplet of spinless Weyl nodes, which are annihilated by spin-orbit coupling. We show that single-crystalline β-Ag_2Se manifests giant Shubnikov–de Haas oscillations in the longitudinal magnetoresistance, which stem from a small electron pocket that can be driven beyond the quantum limit by a field less than 9 T. This small electron pocket is a remainder of the spin-orbit annihilated Weyl nodes and thus encloses a Berry-phase structure. Moreover, we observed a negative longitudinal magnetoresistance when the magnetic field is beyond the quantum limit. Our experimental findings are complemented by thorough theoretical band-structure analyses of this Kramers-Weyl semimetal candidate, including first-principles calculations and an effective $\boldsymbol{k} \cdot \boldsymbol{p}$ model.

DOI: 10.1103/PhysRevB.96.165148

I. INTRODUCTION

Symmetry and topology can cooperate in electronic solids to create low-energy electronic structures with unique properties, resembling Weyl fermions, Dirac fermions, nodal line fermions, and many more [1–14]. The twofold band degeneracy associated with Weyl fermions is the most fundamental, as it is protected by translation symmetry alone and can therefore appear at generic, low-symmetry positions in momentum space. This is indeed the case in all so-called band-inverted Weyl semimetals that have been confirmed experimentally to date.

It has been shown theoretically that there exists a second class of Weyl semimetals in which Weyl nodes are pinned to time-reversal invariant momenta (TRIMs) in the Brillouin zone and cannot move freely in momentum space under small perturbations [12,15]. These Kramers-Weyl nodes appear generically in all chiral crystals, i.e., in crystals that have a sense of handedness by lacking any roto-inversion symmetries [15]. In time-reversal symmetric systems, the Kramers theorem enforces twofold band degeneracy at every TRIM. Spin-orbit coupling (SOC) can in principle split the two Kramers degenerate bands in every direction away from the TRIM, leaving behind a Weyl cone. Roto-inversion and general nonsymmorphic symmetries may prevent the spin-orbit-induced lifting of the band degeneracies along certain directions in momentum space, thereby preventing the Weyl cone formation. In symmorphic chiral crystals, however, every Kramers pair of bands at every TRIM is guaranteed to host a Weyl cone. For nonsymmorphic chiral crystals, the latter is true for a subset of TRIMs only, which, however, always includes the Γ point.

Here, we present a magnetotransport study combined with detailed analyses of the low-energy electronic structure of β-Ag_2Se (naumannite), which is among the first materials that have been theoretically proposed to be a candidate Kramers-Weyl semimetal. β-Ag_2Se crystallizes in a nonsymmorphic chiral structure, and the Fermi pockets are located near the Γ point ($\boldsymbol{k} = \boldsymbol{0}$), where Kramers-Weyl fermions can be expected to reside based on the general symmetry arguments outlined above. We show, however, that an additional set of Fermi pockets is relevant for the low-energy electronic structure of β-Ag_2Se as well, which originates from spinless Weyl nodes that are *annihilated* by SOC—a curious contrast to the Kramers-Weyl nodes *created* by SOC. Our magnetotransport measurements reach the quantum limit (QL) of these Fermi pockets with a magnetic field as low as 3.2 T. In magnetic fields below the QL, we observed giant Shubnikov–de Haas (SdH) oscillations, upon which a nontrivial Berry curvature contributed from the annihilated Weyl fermions is imprinted. Furthermore, we observed a negative longitudinal magnetoresistance (LMR) in a magnetic field beyond the QL. β-Ag_2Se presents a rare example of topological semimetals in which a negative LMR is concomitant with the QL.

II. SYMMETRY AND ELECTRONIC STRUCTURE

Before reporting the experimental results in detail, we discuss the symmetries and electronic structure of β-Ag_2Se.

*gwljiashuang@pku.edu.cn

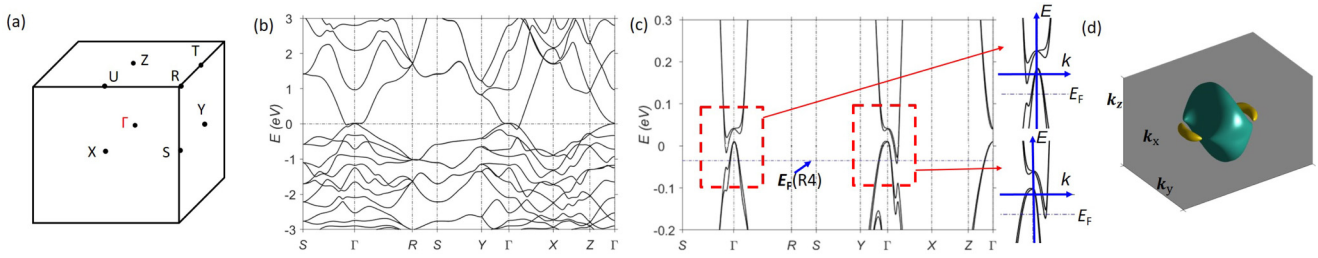

FIG. 1. Band structure of β-Ag_2Se. (a) High-symmetry points in the Brillouin zone of space group $P2_12_12_1$. (b) Band structure without SOC. The band crossings along the $\Gamma-X$ and $\Gamma-Y$ lines are spinless Weyl points with opposite chiral charge. (c) Band structure with SOC. The spinless Weyl nodes annihilate each other when SOC is increased to the physical value. What remains of them are the characteristic extrema of the bands that form electronlike pockets along the $\Gamma-X$ line. In addition, the lifting of the band degeneracy leads to the formation of Kramers Weyl points at each band crossing at the Γ point. Two zoomed-in panels show details on the band structure at the Γ point. (d) Fermi surface maps at energy E_F marked in panel (c). The green Fermi surface encloses a Kramers Weyl point, while the large SdH oscillations measured in this work are attributed to the yellow pockets.

Naumannite crystallizes in the orthorhombic space group 19 ($P2_12_12_1$) with two crystallographically distinct silver atoms and one selenium atom [16,17] (see the upper inset of Fig. 2). Space group 19 has very low symmetry: in addition to time-reversal, it features only three C_2 screw rotations around the principal axes: C_2^x, C_2^y, and C_2^z.

The low-energy band structure of β-Ag_2Se arises entirely from a pair of electron and hole bands around the Γ point [18]. If SOC is neglected [see Fig. 1(b)], these bands are doubly degenerate due to spin, and they carry opposite eigenvalues under the spinless C_2^x and C_2^y rotations. As a consequence, they cannot hybridize along the $\Gamma-X$ and $\Gamma-Y$ lines in the Brillouin zone. Rather, they show a pair of linear crossings along each of these lines. These linear crossings are four spinless Weyl cones, where those on the $\Gamma-X$ line carry opposite chiral charge from those on the $\Gamma-Y$ line. When SOC is included perturbatively, these Weyl degeneracies cannot be lifted due to their chiral charge. Rather, each spinless Weyl node splits into a pair of spinful Weyl nodes that are pinned to the k_x-k_y plane. As SOC increases to the estimated physical value in β-Ag_2Se, spinful Weyl nodes that originated from different spinless Weyl nodes annihilate in the k_x-k_y plane, leaving behind an electronlike Fermi pocket along the $\Gamma-X$ line [Fig. 1(c)].

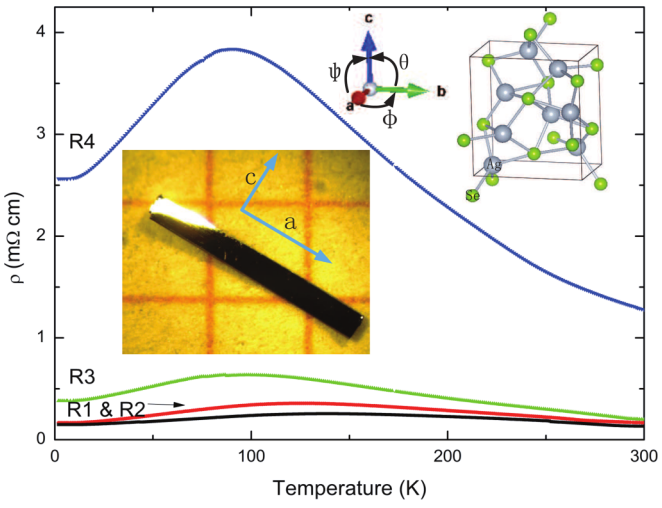

FIG. 2. Temperature-dependent resistivity of four representative β-Ag_2Se single crystals. The resistivity along the **a** direction is similar to the previously reported values in polycrystalline samples with comparable carrier density n [25]. Upper inset: unit cell and definition of angles θ, ϕ, and ψ with respect to the three principal axes. Central inset: a microscopical image of β-Ag_2Se crystal, with scale 1 × 1 mm in the background.

In addition to annihilating the band-inversion Weyl nodes, SOC also creates Kramers-Weyl nodes located at the Γ point. As a consequence, the holelike Fermi surface centered at Γ is split into two sheets [Fig. 1(c)], each of which is fully spin-polarized with a hedgehog spin structure that is pointing toward the Weyl node on one sheet and away from the Weyl node on the other. The hedgehog spin structure is a direct consequence of the topological character of the Weyl node, which is a monopole of Berry curvature in momentum space. The presence of two Fermi pockets in this Kramers-Weyl semimetal, where one encloses the other, obscures some characteristics typically associated with condensed-matter realizations of Weyl fermions. For example, no Fermi-arc states [15] would appear on the surface of β-Ag_2Se. On the other hand, Kramers-Weyl systems uniquely allow us to observe other characteristics of Weyl fermions, not only because of their enhanced symmetry and generic appearance, but also since the Weyl nodes are isolated in energy-momentum space.

A more detailed discussion of an effective $\boldsymbol{k}\cdot\boldsymbol{p}$ model for the Kramers-Weyl node and the spinless Weyl nodes close to the Fermi energy, as well as the symmetry arguments outlined above, can be found in the Appendix.

III. CRYSTAL GROWTH, CHARACTERIZATION, AND EXPERIMENTAL METHODS

In contrast to ample studies on polycrystalline β-Ag_2Se [19–21], there has been no report until now on macrosize single crystals, to the best of our knowledge. Its first-order, polymorphic structural transition at 406 K hinders large single-crystal formation because the cubic α-phase is prone to metamorphosing to a multidomain polycrystalline β-phase during cooling [22,23]. To avoid this roadblock of the structural transition, we designed a single-crystal growth of β-Ag_2Se above 406 K via a modified self-vapor transfer method [24].

Polycrystalline Ag_2Se was ground and sealed in a long fused silica ampoule in vacuum, which was then placed in a

TABLE I. Crystallographic data for β-Ag_2Se.

Space group	$P2_12_12_1$
a (Å)	4.3503(5)
b (Å)	7.0434(10)
c (Å)	7.6779(10)
V (Å^3)	235.26(5)
Z	4
T (K) of data collection	180
Crystal size (mm)	$0.13 \times 0.06 \times 0.04$
Radiation	Mo $K\alpha$ 0.7107 Å
Collection region	$-3 \leqslant h \leqslant 5$
	$-8 \leqslant k \leqslant 8$
	$-9 \leqslant l \leqslant 7$
2θ limit	$3.93^\circ \leqslant 2\theta \leqslant 25.98^\circ$
No. of measured reflections	461
No. of variable parameters	29
R, R_w	0.0626, 0.1503

large temperature gradient from 773 K to near room temperature in a tube furnace for a week. Single crystals of β-Ag_2Se were found near the hot zone where the temperature was presumably about 500–600 K during the growth. The yielded crystals have a ribbonlike shape with a flat hexagonal cross section (central inset of Fig. 2). A close examination under a microscope found that the crystals indeed burgeoned from small seeds of α-phase crystals attached on the inner surface of the ampoule. Single-crystal x-ray diffraction confirmed the crystallographic parameters consistent with previous reports on microsize crystals (Tables I and II). The diffraction also revealed that the long axis of the ribbon is pointing along the crystallographic **a** direction, and the large surface is perpendicular to the **b** direction. Although the structural rearrangement during the α to β phase transition has not been ascertained yet [17], this crystal growth indicates that the β-phase is able to solidify from saturated vapor above the transition temperature.

These macrosized single crystals of β-Ag_2Se allow for a study of the electronic states via transport measurements with of an influence from the scattering from defects, particularly avoiding the grain boundary scattering in polycrystals. In this paper, we focus on the resistivity measurements when the current I is along the crystallographic **a** direction while the magnetic fields are pointing along different directions. (See the upper inset of Fig. 2 for the parametrization of the magnetic-field direction in terms of angles relative to the crystallographic directions.) All physical property characterizations in low fields were performed in a Quantum Design Physical Property measurement system (PPMS-9), adopting the four-wire method.

TABLE II. Atomic parameters and anisotropic thermal vibration parameters for β-Ag_2Se.

Atom	x	y	z	U_{iso}
Ag1	0.1525(4)	0.3839(3)	0.9523(3)	0.0197(6)
Ag2	0.4769(4)	0.2266(3)	0.6357(3)	0.0221(6)
Se	0.1145(5)	0.0034(3)	0.8445(3)	0.0116(6)

$U_{ij} \times 100$

Atom	U_{11}	U_{22}	U_{33}	U_{12}	U_{13}	U_{23}
Ag1	2.25(10)	1.62(11)	2.03(11)	−0.33(9)	−0.46(8)	−0.04(8)
Ag2	2.63(11)	1.49(11)	2.50(11)	−0.40(8)	0.42(7)	−0.63(7)
Se	1.64(10)	0.76(12)	1.07(11)	0.0	0.0	0.0

IV. EXPERIMENT AND DATA ANALYSIS

A. Magnetoresistance at different temperatures

The profile of the temperature-dependent resistivity $\rho(T)$ for the single crystals of β-Ag_2Se is characterized by a broad hump at around 100 K (Fig. 2). This humplike feature in $\rho(T)$ was also observed previously in polycrystals [25,26]. Comparing the four representative samples labeled as R1–R4, we found that the resistivity of samples R1 and R2 from one growth batch is an order of magnitude smaller than that of samples R3 and R4 from a second growth batch. Hall measurements ($I \parallel \mathbf{a}$, $H \parallel \mathbf{b}$) reveal that all samples are n-type for the whole temperature range, and the carrier density is $n = 4.9 \times 10^{19}$ and 2.4×10^{18} cm^{-3} for samples R1 and R4 at 2 K, respectively (see Table III). The n-type carriers likely come from a small amount of deficiencies of selenium atoms, which are commonly observed in other selenide compounds [27]. Both R1 and R4 show a mobility $\mu = 1/\rho ne$ of about 1000 cm^2/V s at 2 K, leading to $\omega_C\tau = \mu B < 1$ at 9 T, where ω_C is the cyclotron frequency and τ is the scattering time.

Figures 3(a) and 3(b) show the magnetoresistance (MR $= \Delta\rho_H/\rho_0$) of the samples R2 and R4 along the three principal axes at different temperatures. The transverse MR for $H \parallel \mathbf{b}$ and **c** for both samples shows a similar profile at different temperatures: the MR crosses over from a quadratic dependence on H at low field to a linear and unsaturated increase up to 9 T. Weak SdH oscillations occur on the linear background when $T < 10$ K and $\mu_0 H > 5$ T for $H \parallel \mathbf{b}$ in R1 and R2 (the samples with larger n), but they are absent in R3 and R4 (the samples with lower n).

At first glance, the profile of LMR for $H \parallel \mathbf{a}$ for R2 seems to be completely different from that for R4 at low temperatures. The LMR for R2 shows strong SdH oscillations up to 9 T, while that for R4 shows weak oscillations in low field, and then it plummets to negative in a magnetic field stronger than 3.2 T. At higher temperatures, the negative LMR survives up to 25 K while the oscillations fade out at 10 K. The data of R2 at different temperatures also have an LMR with SdH oscillations and partially negative shape in high field. Even at 40 K, when the oscillations have faded out completely, the LMR still bends down at 7 T. All of the interesting features can only be observed at low temperatures: the LMRs for both samples degenerate to a small and positive signal when $T > 100$ K.

An analysis of the SdH oscillations for $H \parallel \mathbf{a}$ for different samples sheds light on the ostensible difference of their LMRs. We employed the Lifshitz-Onsager rule for the quantization of the Fermi surface cross-sectional area S_F in R2 and R4 as a function of magnetic field B,

$$S_F \frac{\hbar}{eB} = 2\pi(N + \gamma), \quad (1)$$

TABLE III. Some electrical transport parameters for samples R1–R4. $S_{F,\mathbf{a}}$,$k_{F,\mathbf{a}}$ and $S_{F,\mathbf{b}}$,$k_{F,\mathbf{b}}$ are determined from the SdH frequencies for the fields along the **a** and **b** directions, respectively. E_F and v_F are obtained from the T-dependent amplitude of oscillations for the field along the **a** direction. Blank entries (N/A) signify that the respective quantities have not been measured or observed.

	n (cm^{-3})	$S_{F,\mathbf{a}}$ (T)	$k_{F,\mathbf{a}}$ ($Å^{-1}$)	γ	m^* (m_e)	E_F (meV)	v_F (10^5 ms^{-1})	$S_{F,\mathbf{b}}$ (T)	$k_{F,\mathbf{b}}$ ($Å^{-1}$)
R1	4.9×10^{19}	13.3	0.02	-0.14 ± 0.04	0.1	30	2.3	49	0.039
R2		8.1	0.016	-0.18 ± 0.07	0.075	27	2.5	36	0.033
R3		4.7	0.012	-0.17 ± 0.01				N/A	N/A
R4	2.4×10^{18}	3.8	0.011	-0.18 ± 0.01	0.064	18	2.2	N/A	N/A

where $\hbar$ is the reduced Planck constant, e is the elementary charge, N is the Landau-level (LL) index, and γ is the Onsager phase. The SdH oscillations of R2 originate from a small electron pocket with $S_{F,\mathbf{a}} = 8.1$ T, and the peaks at ± 6.8 T correspond to $N = 1$. For R4, the SdH oscillations originate from an even smaller electron pocket with $S_{F,\mathbf{a}} = 3.8$ T, and a field stronger than 3.2 T drives the system beyond the QL.

Tracing the Landau indices of the SdH oscillations, we find that the negative part of the LMR occurs exactly as long as the system is beyond the QL. From this point of view, the LMRs of R2 and R4 indeed behave similarly if we scale them with respect to the corresponding S_F. We can also conclude that the negative LMR is not a part of the SdH oscillations for all the samples because it survives at higher temperatures than that at which the oscillations are washed out. Above the QL, the LMR of samples R3 and R4 shows a shoulderlike anomaly around 6 T (indicated by the arrows in Fig. 3). This anomaly is always pegged at the fields close to $N = 1/2$ when it is translated to LL indices for various samples with different S_F. The nature of this anomaly is not clear at this point.

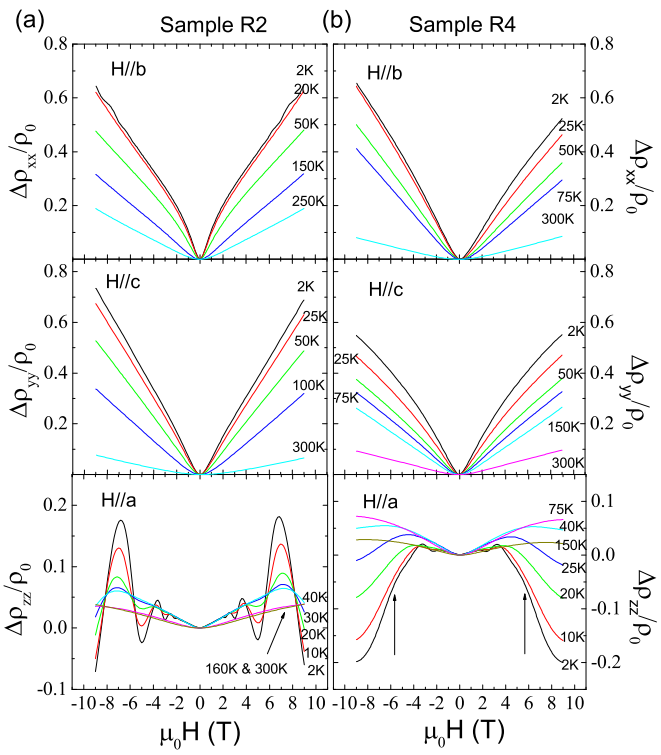

FIG. 3. MR ($\Delta\rho/\rho_0$) for samples R2 (a) and R4 (b) along three principal axes at representative temperatures. From top to bottom: $\Delta\rho_{xx}$, $\Delta\rho_{yy}$, and $\Delta\rho_{zz}$ are for $H \parallel \mathbf{b}$, $\mathbf{c}$, and $\mathbf{a}$, respectively. The arrows in the lower right panel show the shoulderlike anomaly above the QL (see more details in the text).

B. Magnetoresistance at different angles

To map out the electron pockets contributing to the SdH oscillations, we measured the MR for R2 and R4 while the direction of the magnetic field pointed along angles deviating from the three principal axes at 2 K. The MR changes are small when the direction of the field is tilted from along **b** to along **c**. On the other hand, we observed similar patterns of MR changes when the field is tilted from along **a** to along **b** and **c**. Strong SdH oscillations in sample R2 remain pronounced for ϕ and $\psi < 60°$, while the negative part of MR is compensated for by the linear part of the transversal MR when ϕ and $\psi > 30°$ [Figs. 4(a) and 4(b)].

An analysis of the resistivity with respect to the reciprocal of the field projection on the **a** axis is shown in Fig. 5(a). A clear $1/\cos\phi$ and $1/\cos\psi$ dependence up to 60° indicates that the frequencies depend merely on the field component along the **a** direction irrespective of whether the field was tilted toward **b** or **c**. Such an angular dependence is characteristic of an anisotropic ellipsoidlike Fermi pocket. The MR for R4 with a lower oscillation frequency in tilted magnetic field changes in the same manner. This similar angular dependence indicates that the pockets in R4 and R2 are cognate, albeit with different chemical potentials.

A fast Fourier transform (FFT) analysis for the field along different directions can trace subtle changes in the frequencies and map out the shape of the Fermi surface precisely. Angular-dependent extremal orbits on Fermi surfaces are resolved as the frequency peaks in the FFT in Fig. 6. Our analysis reveals that the large frequencies for $H \parallel \mathbf{b}$ and $\mathbf{c}$ indeed stem from the same electron pockets for $H \parallel \mathbf{a}$ with lower frequency. We denote this frequency, which maps out the anisotropic Fermi surface, by α. This result is consistent with the angular-dependent analyses presented above.

V. DISCUSSION

A. Fermi surface

To put the above-mentioned observations in context, we return to the band-structure calculations presented in Fig. 1. We estimated the Fermi level (E_F) by comparing the calculated cross section of the α electron pockets with the measured frequencies for sample R2. The Fermi level is placed at the

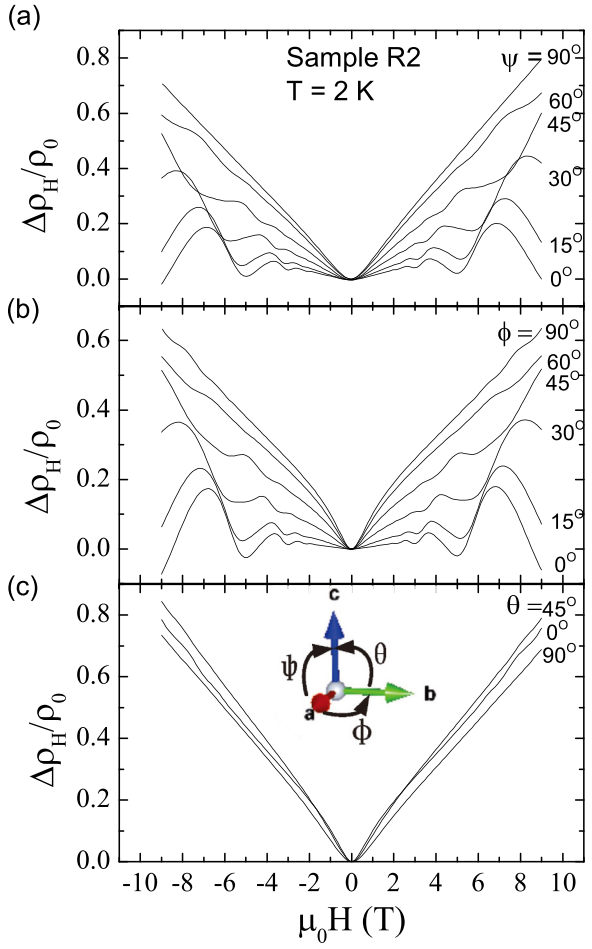

FIG. 4. Anisotropic MR for sample R2 when the direction of the field changes among three principal axes at 2 K. No symmetrization between $\pm H$ was applied.

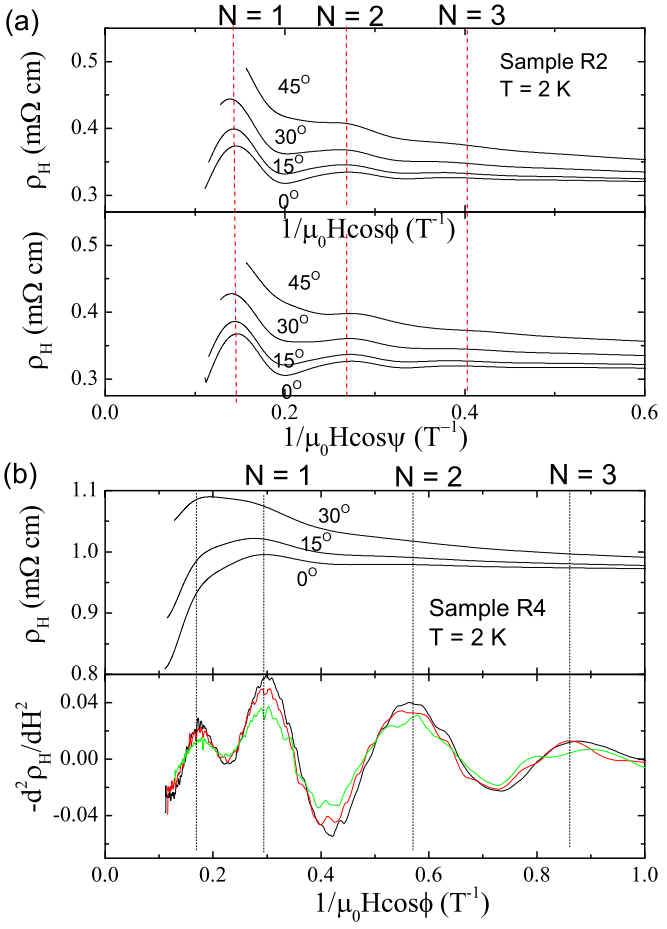

FIG. 5. (a) The resistivity vs $1/\mu_0 H_a = 1/(\mu_0 H\cos\phi)$ and $1/(\mu_0 H\cos\psi)$ for R2 at 2 K. (b) The resistivity and its second derivative vs $1/\mu_0 H_a = 1/(\mu_0 H\cos\phi)$ for R4 at 2 K. The shoulderlike anomaly at $N = 1/2$ is clearly resolved as a peak in the second derivative.

dashed line in Fig. 1(c), while the inferred Fermi surface is shown in Fig. 1(d). Our samples of β-Ag_2Se host a pair of small electronlike kidney-shaped Fermi sheets originating from the gapped spinless Weyl nodes annihilated by SOC [marked in yellow in Fig. 1(d)]. The anisotropy ratios of the calculated Fermi surface cross sections are 3.8 for $S_{\mathrm{F},\mathbf{b}}/S_{\mathrm{F},\mathbf{a}}$ and 4.0 for $S_{\mathrm{F},\mathbf{c}}/S_{\mathrm{F},\mathbf{a}}$. These ratios are consistent with the experimental results shown in Table III. In addition to the electronlike pockets, there are two large holelike Fermi sheets enclosing the Kramers-Weyl point at Γ according to the band-structure calculation [marked in green in Fig. 1(d)]. However, these hole pockets do not show any discerning transport signatures in SdH and Hall measurements. The absence of the contribution from the predicted big hole pockets may be attributed to their low mobility and large effective mass.

Further information about the electron pockets from the spinless Weyl nodes that have been annihilated by SOC can be deduced from the change of the SdH oscillations at different temperatures [28,29]:

$$\rho_H = \rho_0\{1 + A(B,T)\cos[2\pi(S_F/B + \gamma)]\}, \quad (2)$$

where

$$A(B,T) \propto \exp\left(-\frac{2\pi^2 k_B T_D}{\hbar\omega_C}\right)\frac{2\pi^2 k_B T/\hbar\omega_C}{\sinh(2\pi^2 k_B T/\hbar\omega_C)}. \quad (3)$$

In Eq. (3), T_D is the Dingle temperature, k_B is the Boltzmann constant, and the cyclotron frequency $\omega_C = eB/m^*$ (where m^* is the effective mass). Based on Eq. (2), the peak and valley positions of ρ_{zz} are indexed as integers N and half-integers, respectively (because $1/\rho_{zz} = \sigma_{zz} \propto 1/\nu_F$, where ν_F is the density of states at the Fermi level) [30]. Extrapolation of the lines of N versus $1/\mu_0 H$ for all four samples [Fig. 7(a)] leads to the intercepts at $1/\mu_0 H = 0$ clustered around $\gamma = -0.15 \pm 0.05$, despite the fact that $S_{\mathrm{F},\mathbf{a}}$ varies from 13.3 to 3.8 T from sample to sample. This near-zero phase shift, with zero being the alleged value for a 3D Dirac/Weyl semimetal [30–32], may be interpreted as an indication of a nontrivial Berry phase. Our analyses indicate that the annihilation of the spinless Weyl cone does not nullify Berry curvature contributions. The effective mass $m^* = eB/\omega_C$ was obtained from the temperature dependence of the peak amplitude at $N = 1$ for R2 and R4, yielding $0.075m_e$ and $0.064m_e$, respectively [see Fig. 7(b)]. If we assume a linear energy dispersion, we can estimate the Fermi wave vector $k_F = \sqrt{2eS_F/\hbar}$, the Fermi velocity $v_F = \hbar k_F/m^*$, and the Fermi energy $E_F = v_F^2 m^*$ (listed in Table III). The mobility derived from the SdH oscillations is in the order of 10^3 $\mathrm{cm}^2/\mathrm{V\,s}$, comparable with that from the Hall measurements.

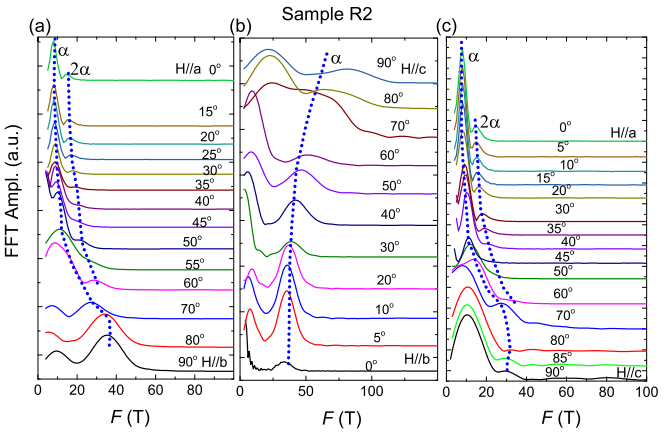

FIG. 6. FFT analysis of SdH oscillations at different angles. Dashed lines show the angular dependence of frequency α. These extra low-field frequency peaks in (b) are ill-shaped and angle-independent, which indicates that they should not be associated with an actual closed cyclotron orbit in β-Ag_2Se.

B. Negative longitudinal magnetoresistance

There is a caveat in the magnetotransport measurements for bulk materials when the magnetic field and current are in parallel [33]: an inhomogeneous distribution of the electric current can induce a MR that is dramatically different from the actual bulk MR of the system. The current jetting effect

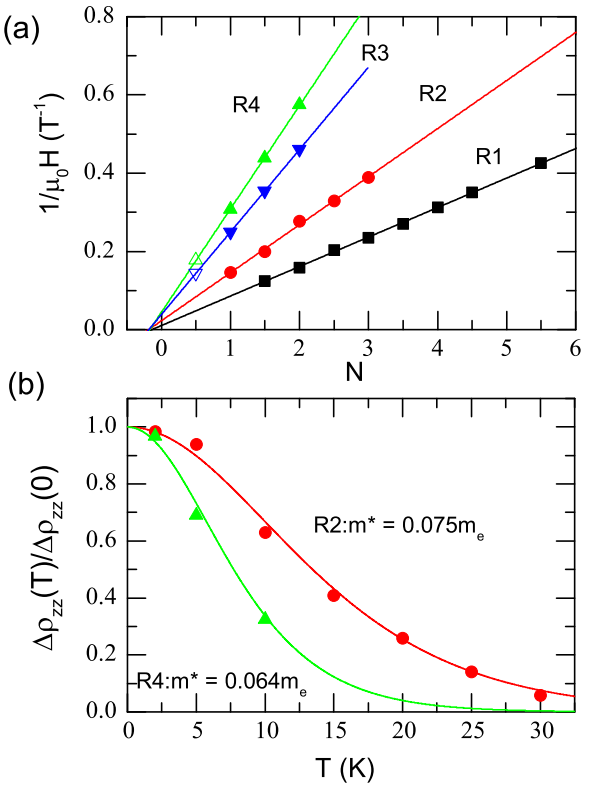

FIG. 7. SdH analyses for LMR for different samples. (a) Landau level indices for all four samples. Two open symbols present the anomaly at $N = 1/2$ for R3 and R4. (b) Temperature dependence of the amplitude of the SdH oscillations at $N = 1$ for R2 and R4.

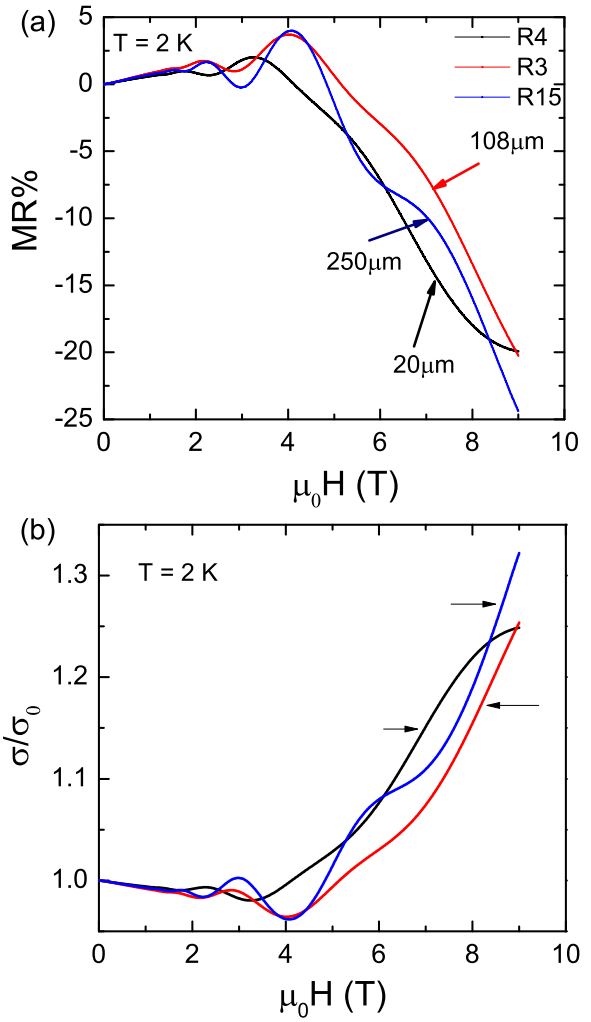

FIG. 8. (a) LMR for three samples of β-Ag_2Se with different thickness taken from the same growth batch. (b) Magnetoconductance for the three samples. The arrows indicate that a linearly dependent magnetoconductance occurs when the field is higher than the position of the shoulderlike anomaly at $N = 1/2$.

in strong magnetic fields when $\omega_C\tau = \mu B \gg 1$ can induce negative LMR in various materials, including polycrystalline silver chalcogenide [34,35]. Such a spurious effect must be excluded before we claim any intrinsic negative LMR in single-crystalline β-Ag_2Se.

To clarify that the current jetting effect is minor and the observed negative LMR in our single-crystalline β-Ag_2Se is intrinsic, we tested several samples with different thickness. Postulating that the negative LMR is merely due to a current distribution in thickness, the measured LMR should differ for these samples. In contrast, as shown in Fig. 8(a), the LMR of three samples behaves very similarly, while their thicknesses vary by one order of magnitude. Figure 8(b) shows the magnetoconductance ($\sigma_{zz} = 1/\rho_{zz}$) for the three samples. We observe a linear field dependence of σ for fields above the shoulderlike anomaly in the QL.

After ruling out a current jetting effect, we try to fathom the origin of the negative LMR in single-crystalline β-Ag_2Se. This concomitant negative part of LMR in the field range

above the QL should stem from the ultraquantum limit of the small electronlike pockets that originate from the spin-orbit annihilated Weyl cones. An Adler-Bell-Jackiw anomaly can cause a linear positive magnetoconductance in the QL for Weyl semimetals [36]. However, a theoretical study taking into account the disorder scattering found that the linear magnetoconductance may also be caused by the interplay of the Landau degeneracy and scattering if v_F and τ depend on the field [37]. In addition to topological semimetals, a topological trivial semiconductor may also bear an H^2-dependent magnetoconductance due to the ionized impurity scattering in a strong magnetic field [38–40]. This complexity in theory makes it difficult to ascribe the negative LMR in β-Ag_2Se to any cogent mechanism, based on our current observation. Nevertheless, we comment that a negative LMR concomitant with the QL in β-Ag_2Se has rarely been reported for any semimetal before.

C. Linear transversal magnetoresistance

Previous studies showed that polycrystalline β-Ag_2Se manifests large, linear-field-dependent, transversal MR in both low- and high-temperature regimes [25,26]. This linear MR remains unsaturated as a function of magnetic-field strength up to 50 T. The origin of this unusual linear MR was interpreted as a quantum effect of electrons attributed to a linear dispersion at the conduction- and valence-band touching points (i.e., a quantum MR) [41,42]. An alternative explanation is that spatial conductivity fluctuations induce a linear MR in these strongly inhomogeneous polycrystals [43,44]. Our measurements on the single crystals may provide new evidence supporting the classical effect. Our band-structure calculation and SdH oscillations reveal that the field in which the linear MR occurs is far less than the QL along the **b** and **c** directions, which is the range of fields in which the presumed quantum MR would be occurring [41,42]. It is noteworthy that the linear MR of the polycrystals in the literature stretches to a much lower field than what we observed for the single crystals. This difference can be well explained by the classical effect in which the stronger spatial conductivity fluctuations in polycrystals lead to more palpable linear MR in a lower field.

VI. CONCLUSION

In summary, we synthesized macrosize single crystals of the Kramers-Weyl semimetal candidate β-Ag_2Se, and we determined its fermiology in detail from SdH oscillations. The dominant SdH signal stems from small non-spin-degenerate and highly anisotropic Fermi surfaces of the bottom of a gapped spinless Weyl cone. As such, these electron pockets inherit a nonvanishing Berry curvature verified as a unified, nontrivial Onsager phase among several samples. A negative LMR concomitant with the QL of these small electron pockets was observed in a strong magnetic field. Finally, we infer that the vapor transfer growth method has great potential for synthesizing single crystals of new materials, especially for thermally unstable compounds.

ACKNOWLEDGMENTS

The authors thank J. Xiong, C. Fang, and F. Wang for helpful discussion, and K. Liu for assistance with TEM measurements. The authors thank J. Wang and Y. Li for using their instruments. S.J. is supported by National Basic Research Program of China (Grant No. 2014CB239302) and National Natural Science Foundation of China (Grant No. 11774007). F.S. acknowledges support from the Swiss National Science Foundation. C.-L.Z. thanks S.-F. Fan for inspiration.

APPENDIX: EFFECTIVE $k \cdot p$ THEORY FOR SPINLESS AND KRAMERS-WEYL POINTS

We want to derive an effective model for the two pairs of bands near the Fermi energy of Ag_2Se that exist near the Γ-point of the Brillouin zone, where each pair is split by SOC. Let us first look at the symmetries of the problem: The space group $P2_12_12_1$ of Ag_2Se is generated by

$$\begin{aligned}(x,y,z) &\to \left(\tfrac{1}{2}+x,\tfrac{1}{2}-y,-z\right)\\ &\to \left(-x,\tfrac{1}{2}+y,\tfrac{1}{2}-z\right)\\ &\to \left(\tfrac{1}{2}-x,-y,\tfrac{1}{2}+z\right).\end{aligned} \tag{A1}$$

In the Bloch basis, the translation operators corresponding to the nonsymmorphic part of the transformations are diagonal in the momenta $(k_x,k_y,k_z)^T = \boldsymbol{k}$, and therefore they do not put constraints on the $\boldsymbol{k}\cdot\boldsymbol{p}$ Hamiltonian $H(\boldsymbol{k})$. We are then left with three independent C_2 rotations:

$$\begin{aligned}C_{2,x}\,\boldsymbol{k}\,C_{2,x}^{-1} &= (k_x,-k_y,-k_z)^T,\\ C_{2,y}\,\boldsymbol{k}\,C_{2,y}^{-1} &= (-k_x,k_y,-k_z)^T,\\ C_{2,z}\,\boldsymbol{k}\,C_{2,z}^{-1} &= (-k_x,-k_y,k_z)^T.\end{aligned} \tag{A2}$$

1. The fate of spinless Weyl points

We first consider the case without SOC, in which the two pairs of bands around Γ remain spin-degenerate. From the first-principles calculation, we know that they have the same $C_{2,z}$ eigenvalue along the k_z axis and opposite eigenvalues under $C_{2,x}$ and $C_{2,y}$ along the k_x and k_y axis, respectively. Henceforth, we can choose, without loss of generality, the representations

$$R_{2,x}=\tau_x,\quad R_{2,y}=\tau_x,\quad R_{2,z}=\mathbb{1}_2, \tag{A3}$$

where $\tau_{x,y,z}$ are the three Pauli matrices and $\mathbb{1}_2$ is the 2×2 unit matrix. This spinless representation obeys $R_{2,x}R_{2,y}=R_{2,z}$, as it should.

Spinless time-reversal symmetry is given by $T=K$, where K is complex conjugation. Furthermore, we have $T\,\boldsymbol{k}\,T^{-1}=-\boldsymbol{k}$, since flipping the direction of time reverses all velocities. The most general spinless Hamiltonian that obeys both time reversal and the three twofold rotation symmetries is, to second order in $\boldsymbol{k}$, given by

$$H_0=\left(w_xk_x^2+w_yk_y^2+w_zk_z^2-m\right)\tau_x+ak_z\tau_y+bk_xk_y\tau_z. \tag{A4}$$

Note that we have neglected the term proportional to the identity matrix, which is irrelevant for the discussion of symmetry- or topology-enforced band degeneracies. Hamiltonian (A4) asymptotically describes an electron and a hole band. The Hamiltonian can feature up to four spinless Weyl points at the points in momentum space where each of the terms vanishes

individually. For $w_x, w_y, w_z, m > 0$, the first term vanishes on an ellipsoid in momentum space. The intersections of this ellipsoid with the k_x and k_y axis are the locations of the four Weyl points. This is in agreement with the observation from our DFT calculation, which exhibits these Weyl points if SOC is neglected.

We will now discuss how these Weyl points are perturbed if SOC is switched on. It is clear that due to their chiral nature, infinitesimal perturbations cannot gap them out immediately, but rather split them in momentum space. If the spin space is acted on with the three Pauli matrices $\sigma_{x,y,z}$, the symmetries are now represented as follows. Time reversal is implemented by the operator $T = Ki\sigma_y$. The spinful rotation operations are given by

$$R_{2,x} = i\tau_x \otimes \sigma_x, \quad R_{2,y} = i\tau_x \otimes \sigma_y, \quad R_{2,z} = i\mathbb{1}_2 \otimes \sigma_z. \tag{A5}$$

We will only consider SOC terms up to linear order in $\boldsymbol{k}$. Obviously, there is no single SOC term that anticommutes with all terms forming a Weyl cone in Hamiltonian (A4). This is in accordance with our expectation that infinitesimal SOC cannot gap out the Weyl nodes. The following SOC terms are symmetry-allowed:

$$\begin{aligned} H_{\mathrm{SOC}} = {} & \lambda_1\, \tau_y \otimes \sigma_z + \lambda_2\, k_x \mathbb{1}_2 \otimes \sigma_x + \lambda_3\, k_x \tau_x \otimes \sigma_x \\ & + \lambda_4\, k_x \tau_z \otimes \sigma_y + \lambda_5\, k_y \mathbb{1}_2 \otimes \sigma_y + \lambda_6\, k_y \tau_x \otimes \sigma_y \\ & + \lambda_7\, k_y \tau_z \otimes \sigma_x + \lambda_8\, k_z \mathbb{1}_2 \otimes \sigma_z + \lambda_9\, k_z \tau_x \otimes \sigma_3. \end{aligned} \tag{A6}$$

Of these, the λ_2, λ_5, and λ_8 terms commute with the entire Hamiltonian (A4) and, therefore, they do not *per se* lead to any change in the position of the Weyl nodes, but spin-split them in energy. The remaining terms, each on their own, have the following impact: The λ_1 term splits each of the four spinless Weyl nodes into two Weyl nodes separated in the k_z direction. The λ_3 term splits each of the two spinless Weyl nodes on the k_x axis into two Weyl nodes separated in the k_x direction. The λ_4 term splits each of the two spinless Weyl nodes on the k_x axis into two Weyl nodes separated in the k_y direction. The λ_6 term splits each of the two spinless Weyl nodes on the k_y axis into two Weyl nodes separated in the k_y direction. The λ_7 term splits each of the two spinless Weyl nodes on the k_y axis into two Weyl nodes separated in the k_x direction. In summary, the SOC terms have the potential to split each of the spinless Weyl points into two Weyl nodes along the k_x, k_y, or k_z direction. Time-reversal and rotation symmetries pin the Weyl nodes to lie in quadruplets on the high-symmetry planes k_x-k_y, k_y-k_z, or k_x-k_z.

As evidenced by our first-principles calculation, however, SOC in Ag_2Se is strong enough to gap out the Weyl nodes by annihilating them. As SOC is gradually increased, each spinless Weyl node splits into two Weyl nodes that separate in a way corresponding to dominant λ_4 and λ_7 terms in the $\boldsymbol{k} \cdot \boldsymbol{p}$ model. When SOC reaches the physical value it has in Ag_2Se, Weyl nodes that originated from different spinless Weyl cones have annihilated pairwise, and there is a direct gap between the second and third bands in all of momentum space.

2. Emergence of Kramers-Weyl points

We have largely neglected the discussion of the terms proportional to λ_2, λ_5, and λ_8 as they commute with the Hamiltonian (A4). They do, however, have an important effect on the spin-splitting of an individual band: Isolated Weyl nodes emerge in the form of Kramers degeneracies of *every* pair of bands at the Γ point in momentum space.

To show this within a $\boldsymbol{k} \cdot \boldsymbol{p}$ expansion, we focus on a single pair of bands only [as compared to two pairs of bands in Hamiltonian (A4)]. The effective Hamiltonian $H(\boldsymbol{k})$ should be invariant under all C_2 rotations, as well as time-reversal. As for any two-dimensional matrix, we can write it as a linear combination of the identity and σ-matrices. In an expansion around the Γ-point in powers of the individual components of $\boldsymbol{k}$, time-reversal symmetry excludes odd powers for the coefficient of $\mathbb{1}_2$ and even powers for the coefficients of the σ-matrices. The C_2 rotation symmetries imply that every component of $\boldsymbol{k}$ has to be paired up with the same component of $\boldsymbol{\sigma}$, or with itself. To second order in $\boldsymbol{k}$, the Hamiltonian is then given by

$$\begin{aligned} H(\boldsymbol{k}) = {} & v_x k_x\, \sigma_x + v_y k_y\, \sigma_y + v_z k_z\, \sigma_z \\ & + \left(u_x k_x^2 + u_y k_y^2 + u_z k_z^2\right) \mathbb{1}_2. \end{aligned} \tag{A7}$$

So just by symmetry, the band structure always contains a Weyl point at $\boldsymbol{k} = \boldsymbol{0}$.

This result is in qualitative agreement with our DFT calculation for Ag_2Se. We can determine the coefficients from the DFT calculation, for the lower pair of bands that cross the Fermi level, as

$$\begin{aligned} & v_x = 0.079\ \mathrm{eV\,\AA}, \quad v_y = 0.066\ \mathrm{eV\,\AA}, \quad v_z = 0.020\ \mathrm{eV\,\AA}, \\ & u_x = -14.8\ \mathrm{eV\,\AA}^2, \quad u_y = -2.97\ \mathrm{eV\,\AA}^2, \\ & u_z = -1.55\ \mathrm{eV\,\AA}^2. \end{aligned} \tag{A8}$$

The Chern numbers of the two Fermi surfaces are exactly opposite, and there are no Fermi arcs visible on any surface.

[1] X. Wan, A. M. Turner, A. Vishwanath, and S. Y. Savrasov, Topological semimetal and Fermi-arc surface states in the electronic structure of pyrochlore iridates, Phys. Rev. B **83**, 205101 (2011).

[2] L. X. Yang, Z. K. Liu, Y. Sun, H. Peng, H. F. Yang, T. Zhang, B. Zhou, Y. Zhang, Y. F. Guo, M. Rahn *et al.*, Weyl semimetal phase in the non-centrosymmetric compound TaAs, Nat. Phys. **11**, 728 (2015).

[3] S.-M. Huang, S.-Y. Xu, I. Belopolski, C.-C. Lee, G. Chang, B. Wang, N. Alidoust, G. Bian, M. Neupane, C. Zhang *et al.*, A Weyl fermion semimetal with surface Fermi arcs in the transition metal monopnictide TaAs class, Nat. Commun. **6**, 7373 (2015).

[4] H. Weng, C. Fang, Z. Fang, B. A. Bernevig, and X. Dai, Weyl Semimetal Phase in Noncentrosymmetric Transition-Metal Monophosphides, Phys. Rev. X **5**, 011029 (2015).

[5] B. Q. Lv, H. M. Weng, B. B. Fu, X. P. Wang, H. Miao, J. Ma, P. Richard, X. C. Huang, L. X. Zhao, G. F. Chen, Z. Fang, X. Dai, T. Qian, and H. Ding, Experimental Discovery of Weyl Semimetal TaAs, Phys. Rev. X **5**, 031013 (2015).

[6] S.-Y. Xu, I. Belopolski, N. Alidoust, M. Neupane, G. Bian, C. Zhang, R. Sankar, G. Chang, Z. Yuan, C.-C. Lee, S.-M. Huang, H. Zheng, J. Ma, D. S. Sanchez, B. Wang, A. Bansil, F. Chou, P. P. Shibayev, H. Lin, S. Jia, and M. Z. Hasan, Discovery of a Weyl fermion semimetal and topological fermi arcs, Science **349**, 613 (2015).

[7] A. A. Burkov, M. D. Hook, and L. Balents, Topological nodal semimetals, Phys. Rev. B **84**, 235126 (2011).

[8] G. Bian, T.-R. Chang, R. Sankar, S.-Y. Xu, H. Zheng, T. Neupert, C.-K. Chiu, S.-M. Huang, G. Chang, I. Belopolski *et al.*, Topological nodal-line fermions in spin-orbit metal $PbTaSe_2$, Nat. Commun. **7**, 10556 (2016).

[9] L. M. Schoop, M. N. Ali, C. Straßer, A. Topp, A. Varykhalov, D. Marchenko, V. Duppel, S. S. P. Parkin, B. V. Lotsch, and C. R. Ast, Dirac cone protected by non-symmorphic symmetry and three-dimensional dirac line node in ZrSiS, Nat. Commun. **7**, 11696 (2016).

[10] M. Neupane, I. Belopolski, M. M. Hosen, D. S. Sanchez, R. Sankar, M. Szlawska, S.-Y. Xu, K. Dimitri, N. Dhakal, P. Maldonado, P. M. Oppeneer, D. Kaczorowski, F. Chou, M. Z. Hasan, and T. Durakiewicz, Observation of topological nodal fermion semimetal phase in ZrSiS, Phys. Rev. B **93**, 201104 (2016).

[11] C.-L. Zhang, Z. Yuan, G. Bian, S.-Y. Xu, X. Zhang, M. Z. Hasan, and S. Jia, Superconducting properties in single crystals of the topological nodal semimetal $PbTaSe_2$, Phys. Rev. B **93**, 054520 (2016).

[12] B. Bradlyn, J. Cano, Z. Wang, M. G. Vergniory, C. Felser, R. J. Cava, and B. A. Bernevig, Beyond Dirac and Weyl fermions: Unconventional quasiparticles in conventional crystals, Science **353**, aaf5037 (2016).

[13] A. A. Soluyanov, D. Gresch, Z. Wang, Q. Wu, M. Troyer, X. Dai, and B. A. Bernevig, Type-ii weyl semimetals, Nature (London) **527**, 495 (2015).

[14] Z. Wang, A. Alexandradinata, R. J. Cava, and B. A. Bernevig, Hourglass fermions, Nature (London) **532**, 189 (2016).

[15] G. Chang, D. S. Sanchez, B. J. Wieder, S.-Y. Xu, F. Schindler, I. Belopolski, S.-M. Huang, B. Singh, D. Wu, T. Neupert *et al.*, Kramers theorem-enforced Weyl fermions: Theory and materials predictions, arXiv:1611.07925.

[16] G. A. Wiegers, The crystal structure of the low-temperature form of silver selenide, Am. Miner. **56**, 1882 (1971).

[17] H. Billetter and U. Ruschewitz, Structural phase transitions in Ag_2Se (naumannite), Z. Anorg. Allg. Chem. **634**, 241 (2008).

[18] W. Zhang, R. Yu, W. Feng, Y. Yao, H. Weng, X. Dai, and Z. Fang, Topological Aspect and Quantum Magnetoresistance of β-Ag_2Te, Phys. Rev. Lett. **106**, 156808 (2011).

[19] Z. Zhao, S. Wang, A. R. Oganov, P. Chen, Z. Liu, and W. L. Mao, Tuning the crystal structure and electronic states of Ag_2Se: Structural transitions and metallization under pressure, Phys. Rev. B **89**, 180102 (2014).

[20] B. Gates, Y. Yin, P. Yang, and Y. Xia, Single-crystalline nanowires of Ag_2Se can be synthesized by templating against nanowires of trigonal Se, J. Am. Chem. Soc. **123**, 11500 (2001).

[21] J. Yu and H. Yun, Reinvestigation of the low-temperature form of Ag_2Se (naumannite) based on single-crystal data, Acta Crystallogr. Sect. E **67**, i45 (2011).

[22] P. Rahlfs, The cubic high temperature modificators of sulfides, selenides and tellurides of silver and of univalent copper, Z. Phys. Chem. B **31**, 157 (1936).

[23] Y. Kumashiro, T. Ohachi, and I. Taniguchi, Phase transition and cluster formation in silver selenide, Solid State Ion. **86**, 761 (1996).

[24] A. Szczerbakow and K. Durose, Self-selecting vapour growth of bulk crystals—Principles and applicability, Prog. Cryst. Growth Char. Mater. **51**, 81 (2005).

[25] R. Xu, A. Husmann, T. F. Rosenbaum, M.-L. Saboungi, J. E. Enderby, and P. B. Littlewood, Large magnetoresistance in non-magnetic silver chalcogenides, Nature (London) **390**, 57 (1997).

[26] A. Husmann, J. B. Betts, G. S. Boebinger, A. Migliori, T. F. Rosenbaum, and M.-L. Saboungi, Megagauss sensors, Nature (London) **417**, 421 (2002).

[27] S. Jia, H. Ji, E. Climent-Pascual, M. K. Fuccillo, M. E. Charles, J. Xiong, N. P. Ong, and R. J. Cava, Low-carrier-concentration crystals of the topological insulator Bi_2Te_2Se, Phys. Rev. B **84**, 235206 (2011).

[28] D. Shoenberg, *Magnetic Oscillations in Metal* (Cambridge University Press, Cambridge, 2009).

[29] G. Landwehr and E. I. Rashba, *Landau Level Spectroscopy* (North-Holland, Amsterdam, 1991), Vol. 27.2.

[30] C. M. Wang, H.-Z. Lu, and S.-Q. Shen, Anomalous Phase Shift of Quantum Oscillations in 3D Topological Semimetals, Phys. Rev. Lett. **117**, 077201 (2016).

[31] G. P. Mikitik and Yu. V. Sharlai, Berry phase and the phase of the Shubnikov–de Haas oscillations in three-dimensional topological insulators, Phys. Rev. B **85**, 033301 (2012).

[32] H. Murakawa, M. S. Bahramy, M. Tokunaga, Y. Kohama, C. Bell, Y. Kaneko, N. Nagaosa, H. Y. Hwang, and Y. Tokura, Detection of Berry's phase in a bulk Rashba semiconductor, Science **342**, 1490 (2013).

[33] A. B. Pippard, *Magnetoresistance in Metals* (Cambridge University Press, Cambridge, 2009).

[34] J. Hu, T. F. Rosenbaum, and J. B. Betts, Current Jets, Disorder, and Linear Magnetoresistance in the Silver Chalcogenides, Phys. Rev. Lett. **95**, 186603 (2005).

[35] X.-T. Xu and S. Jia, Recent observations of negative longitudinal magnetoresistance in semimetal, Chin. Phys. B **25**, 117204 (2016).

[36] H. B. Nielsen and M. Ninomiya, The Adler-Bell-Jackiw anomaly and Weyl fermions in a crystal, Phys. Lett. B **130**, 389 (1983).

[37] H.-Z. Lu and S.-Q Shen, Quantum transport in topological semimetals under magnetic fields, Front. Phys. **12**, 127201 (2017).

[38] P. N. Argyres and E. N. Adams, Longitudinal magnetoresistance in the quantum limit, Phys. Rev. **104**, 900 (1956).

[39] P. N. Argyres, Galvanomagnetic effects in the quantum limit, J. Phys. Chem. Solids **8**, 124 (1959).

[40] P. Goswami, J. H. Pixley, and S. Das Sarma, Axial anomaly and longitudinal magnetoresistance of a generic three-dimensional metal, Phys. Rev. B **92**, 075205 (2015).

[41] A. A. Abrikosov, Quantum magnetoresistance, Phys. Rev. B **58**, 2788 (1998).

[42] A. A. Abrikosov, Quantum linear magnetoresistance, Europhys. Lett. **49**, 789 (2000).

[43] M. M. Parish and P. B. Littlewood, Non-saturating magnetoresistance in heavily disordered semiconductors, Nature (London) **426**, 162 (2003).

[44] J. Hu and T. F. Rosenbaum, Classical and quantum routes to linear magnetoresistance, Nat. Mater. **7**, 697 (2008).